Neutral thermospheric dynamics observed with two scanning Doppler imagers: 3. Horizontal wind gradients

C. Anderson,[1] M. Conde,[1] and M. G. McHarg[2]

Received 21 December 2011; revised 2 February 2012; accepted 21 March 2012; published 10 May 2012.

[1] This is the third and final article in a series of papers reporting on observations of the 630.0 nm thermospheric airglow emission by two spatially separated scanning Doppler imagers (SDI's) in Alaska. In this article, bistatic winds derived from the combined measurements of both instruments in a region of field-of-view overlap were used to derive local-scale maps of horizontal neutral wind gradients. Averaged over the bistatic 'field-of-view', these gradient estimates were compared with the monostatic gradient estimates routinely produced by the two SDI's. The key findings to emerge from this study include: 1) the bistatic gradient estimate agreed very well with monostatic estimates for the majority of the time which, given the very different methods involved in each technique, gives us great confidence in our ability to measure F-region neutral wind gradients; 2) the strongest gradient was that which describes the magnetic meridional shear of the zonal wind, which is driven by momentum deposition from convecting ions; 3) vortical flow was more often observed than divergent flow, and both types of flow showed systematic variations with magnetic local time; 4) viscous heating due to non-negligible gradients was on the order of 10^{-11} Wm^{-3} which, while small compared to typical F-region Joule heating rates, may be comparable to particle heating, and in a time-integrated sense may be an appreciable source of heating.

Citation: Anderson, C., M. Conde, and M. G. McHarg (2012), Neutral thermospheric dynamics observed with two scanning Doppler imagers: 3. Horizontal wind gradients, *J. Geophys. Res.*, *117*, A05311, doi:10.1029/2011JA017471.

1. Introduction

[2] Spatial derivatives of the velocity field play important roles in the equations governing atmospheric dynamics and energetics. They are present in the non-linear advection terms which describe bulk transport of mass, energy and momentum, and which give rise to many of the complex phenomena associated with fluid mechanics [*Davidson*, 2004]. Gradients affect momentum transport through the diffusive action of viscosity, and the dissipation of mechanical energy again through the action of viscosity. They also appear (through products of velocity perturbations) in terms describing turbulent momentum flux.

[3] Horizontal neutral winds in the thermosphere are often assumed to be relatively uniform over horizontal scales of 1000 km or less, which is typically comparable to the effective field-of-view of ground-based Fabry-Perot interferometers. This is not an unreasonable assumption given that the neutral thermosphere possesses a large kinematic viscosity owing to its high temperature and low mass density, and is driven (in a globally averaged sense) predominantly by large-scale pressure gradients resulting from solar insolation.

[4] However, it has long been known [e.g., *Cole*, 1962, 1971; *Meriwether et al.*, 1973] that at auroral latitudes the neutral thermosphere can be strongly influenced by magnetospheric processes and by interactions with the ionospheric plasma, both in terms of momentum transfer from collisions with the fast moving ions, and energy deposition from such processes as Joule and particle heating. One result of these interactions is the formation of structures in the neutral thermospheric wind field at scales on the order of 100 km, scales which have only recently begun to be considered important.

[5] Indeed observations of highly structured neutral wind fields at auroral latitudes have been around for many years, as for example those reported by *Wu et al.* [1974] or from the Dynamics Explorer satellites [*Killeen et al.*, 1982; *Spencer et al.*, 1982; *Hays et al.*, 1984; *Killeen et al.*, 1984; *Killeen and Roble*, 1988]. One striking feature of these observations were the strong latitudinal gradients of the zonal wind, with sharp reversals in wind direction over only two or three degrees of latitude. Similar observations from ground-based instruments have been reported by *Conde and Smith* [1998], *Conde et al.* [2001] and *Anderson et al.* [2011a]. These types of zonal wind shears are made possible by correspondingly sharp gradients in plasma velocities.

[1]Geophysical Institute, University of Alaska, Fairbanks, Alaska, USA.
[2]Physics Department, U.S. Air Force Academy, Colorado Springs, Colorado, USA.

Corresponding author: C. Anderson, Geophysical Institute, University of Alaska Fairbanks, Fairbanks, AK 99775, USA. (callum@gi.alaska.edu)

0148-0227/12/2011JA017471

[6] Proper measurement of wind gradients depends on both good spatial sampling and concurrency. In order to separate temporal and spatial variations, it is necessary to complete a spatial sampling of the velocity field (at multiple locations) with a time resolution at least comparable to the time-scales at which changes in the wind field are driven. Depending on their time resolution, some narrow-field instruments may not be able to satisfy this requirement all the time. However, scanning Doppler imagers (SDIs) do meet this requirement [*Conde and Smith*, 1998; *Griffin et al.*, 2008], as they have fast optics and sample the wind field at multiple locations (in the present work, 115 locations) across the sky simultaneously.

[7] With a single SDI, the usual monostatic vector wind fitting technique [*Conde and Smith*, 1998] is able to generate estimates of three of the four first-order wind gradients from the azimuthal variation of the line-of-sight wind speed. This calculation can be used to directly estimate the two gradients describing divergence, however only one equation relates the two gradients describing shear to observed parameters (see section 3.1). Thus an assumption must be made about one of the shear gradients (or it must be estimated independently) before an estimate of the other shear gradient can be obtained, and this is a limitation of the technique.

[8] Recent work by *Anderson et al.* [2011a] has shown that bistatic wind imaging using two SDI's with overlapping fields-of-view can be used to resolve structure at smaller spatial scales than is possible with a single instrument due to the greatly reduced set of assumptions required for inferring a given horizontal wind vector. Using the bistatic imaging technique, wind speed estimates made within a common-volume are local to that volume, and do not rely on information from other locations across the sky (as they do for example when fitting monostatic wind fields). Finite differencing of these wind estimates can be used to estimate all four gradients (see section 3.2). Bistatic imaging therefore provides us with an independent method of inferring all four horizontal wind gradients, which can be compared with the gradients that have been routinely calculated as part of the monostatic fitting technique.

[9] Previous measurements of thermospheric neutral wind gradients include those by *Burnside et al.* [1981] and *Friedman and Herrero* [1982] at Arecibo (18.3°N, MLAT 28°), where the strongest gradients, with magnitudes up to 0.3×10^{-3} s^{-1}, were meridional, and associated with the post-midnight wind reversal (note that 10^{-3} s^{-1} is equivalent to 1 ms^{-1} km^{-1}). *Biondi* [1984] reported a meridional gradient of 0.08×10^{-3} s^{-1} from Laurel Ridge (40.1°N, MLAT 35.1°). *Smith and Hernandez* [1995] reported values of total horizontal divergence between $\pm$ 1.0×10^{-3} s^{-1} above South Pole station (90°S, MLAT 75°) in Antarctica, and *Guo and McEwen* [2003] reported values between -0.2 and 0.1×10^{-3} s^{-1} from Eureka (80.1°N, MLAT 88.9°), in the northern hemisphere central polar cap.

[10] *Greet et al.* [1999] presented observations of the thermospheric wind field above Mawson and Davis stations in Antarctica, and appreciable wind gradients were frequently present in the wind fields they showed. These wind fields were derived from eight line-of-sight wind measurements (four from each of the Mawson and Davis instruments), with a time resolution of 40 min to 1 hour for a complete set of sky measurements. The strongest gradients apparent in the graphical wind fields shown by *Greet et al.* [1999] were frequently in the magnetic meridional direction, however no quantitative gradient estimates were presented by these authors.

[11] Average zonal gradients of approximately 0.06×10^{-3} s^{-1} were reported by *Aruliah and Griffin* [2001] using narrow-field Fabry-Perot interferometer data from Kiruna, Sweden. The fact that these gradients were present in the averaged data strongly indicated that they were a persistent feature of the wind field. Tristatic FPI measurements made in conjunction with tristatic radar have further highlighted the importance of incorporating meso-scale ion-neutral variability into calculations of Joule heating [e.g., *Aruliah et al.*, 2004, 2005].

[12] This work is a continuation of the bistatic analyses presented in *Anderson et al.* [2011a] and *Anderson et al.* [2011b] (hereafter referred to as Papers 1 and 2, respectively). In this article, gradients derived from both monostatic and bistatic wind measurements are compared, and the assumptions underlying the monostatic wind fitting technique (which are not present in the bistatic method) are tested. The statistical distributions of F-region neutral wind field gradients are examined, and the impact of these gradients on neutral heating (through viscous dissipation of mechanical energy) is calculated.

2. Instrumentation

[13] The two instruments used in this study were described in Paper 1. These are two all-sky scanning Doppler imagers which are capable of recording independent airglow spectra from 115 locations simultaneously across the sky. One of these instruments operates at Poker Flat, Alaska, and is owned by the Geophysical Institute. The second instrument is located at Gakona, Alaska, and is owned by the United States Air Force Academy. The locations of these instruments are shown in Figure 1.

3. Analysis

3.1. Monostatic Gradients

[14] As part of the process that fits a horizontal vector wind field to a set of monostatic wind measurements (described in Paper 1; also see *Conde and Smith* [1998]), gradients of the zonal and meridional wind are calculated from the Fourier coefficients describing the azimuthal variation of the line-of-sight wind around a single annulus of zones. Let the horizontal wind vector be labeled $\mathbf{v} = (v_x, v_y)$, with components in the zonal (x) and meridional (y) directions. The equations that relate the gradients describing the divergence of the wind field ($\partial v_x/\partial x$ and $\partial v_y/\partial y$) to the calculated Fourier coefficients form a complete set, and can thus be solved uniquely for these gradients. However, only one equation relates the gradients describing shear ($\partial v_x/\partial y$ and $\partial v_y/\partial x$) to measured parameters. Thus an assumption must be made regarding the value of one of these shear gradients in order to solve for the other.

[15] As described in Paper 1, the assumption made in this work is that the zonal gradient of the meridional wind ($\partial v_y/\partial x$,

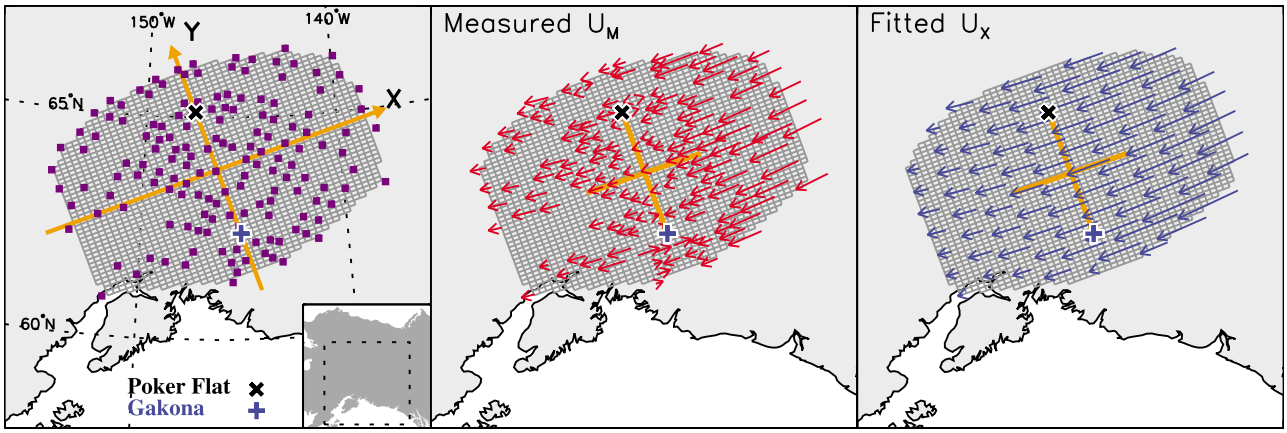

Figure 1. (left) Purple squares show the locations of bistatic measurement volumes as described in *Anderson et al.* [2011a]. Grey lines indicate the orientation of the grid used for discretization (see text). Horizontal coordinate axes x and y for the grid are also shown, along with the locations of the Poker Flat and Gakona instruments. (middle) The raw measured u_m component of the bistatic wind. (right) The u_x values fitted to the gridded u_m with the weighted least squares fit described in text. Note that u_x is calculated at every grid location, but is displayed at lower resolution in this figure for clarity.

in geomagnetic coordinates) is zero. The remaining wind gradient can then be calculated from:

$$\frac{\partial v_x}{\partial y} = \frac{2b_2}{R} - \frac{\partial v_y}{\partial x} \tag{1}$$

where b_2 is the Fourier coefficient describing the second harmonic variation of the sinusoidal component of the line-of-sight wind, R is the horizontal radius of the measurement annulus (centered on the station zenith), and as described above $\partial v_y/\partial x$ is here set equal to zero (the reader is referred to *Conde and Smith* [1998] for a detailed discussion of this technique and the origin of equation (1)). Since a gradient can be estimated in each annulus containing 6 or more zones, gradients are typically averaged across all such annuli to produce an all-sky average. Monostatic gradients shown in this article represent the median value across all annuli (not including the central zone).

3.2. Bistatic Gradients

[16] The derivation of bistatic horizontal wind vectors was described in detail in Paper 1. Bistatic wind components are uniquely resolved along two orthogonal axes lying in the 'viewing plane', that is the plane whose normal is given by the cross-product of the lines-of-sight from each station to the common-volume location under consideration. One of these axes, labeled $\hat{\mathbf{l}}$, is horizontal and parallel to the great circle direction from Gakona to Poker Flat (positive in the direction of increasing latitude). The second axis is labeled $\hat{\mathbf{m}}$, and has a horizontal component along the direction perpendicular to $\hat{\mathbf{l}}$, and a non-zero component in the local vertical direction, the magnitude of which depends on the distance of the common-volume from the Poker-Gakona great circle. Let $\mathbf{u} = (u_m, u_l)$ be the bistatically measured wind vector with components along each of the $\hat{\mathbf{l}}$ and $\hat{\mathbf{m}}$ axes.

[17] While the $\hat{\mathbf{l}}$-axis has a constant absolute orientation at every common-volume location, and has no vertical component, the absolute orientation of the $\hat{\mathbf{m}}$-axis is in general different for different common-volumes. For volumes lying close to the Poker-Gakona great circle, the $\hat{\mathbf{m}}$-axis has a large vertical component, and thus the u_m component of the bistatic wind measured at these locations is dominated by the vertical wind. In volumes lying farther from the great circle, the horizontal wind component begins to dominate. For the figures presented in Paper 1, only those bistatic locations for which the angle between the $\hat{\mathbf{m}}$-axis and the local vertical was greater than 30° were displayed, since at smaller angles the vertical wind contribution to the u_m component would be undesirably large (note that the u_l component is unaffected by common-volume location).

[18] In order to calculate gradients from the bistatic measurements, we adopted a finite difference approach. The first step was to discretize the measurement domain into a regular (square) grid, as shown in Figure 1. The left panel of this figure shows a set of bistatic measurement locations as purple squares, plotted on a zoomed-in map of Alaska. In this article, a fitting technique (described below), which makes use of all available bistatic data, was used to estimate the horizontal component of the bistatic wind. Therefore, unlike Paper 1, data from all bistatic locations will be used regardless of distance from the Gakona/Poker Flat great circle, and thus all bistatic volumes are shown in Figure 1. The inset map in the bottom right corner of the panel shows the map orientation. Thin grey lines in the main panel depict the discretized domain, with 50 grid points in each direction. Grid coordinate axes are labeled X and Y as shown in the figure, and the locations of the Gakona and Poker Flat SDI's are marked. The X-axis origin is located where it intersects the Gakona/Poker Flat great circle, the Y-axis origin is midway between Gakona and Poker Flat. The XY coordinate system of the bistatic grid is related to the xy monostatic coordinate system by an anti-clockwise rotation of 40°, that is:

$$\begin{pmatrix} X \\ Y \end{pmatrix} = \begin{pmatrix} \cos(40^\circ) & -\sin(40^\circ) \\ \sin(40^\circ) & \cos(40^\circ) \end{pmatrix} \begin{pmatrix} x \\ y \end{pmatrix} \tag{2}$$

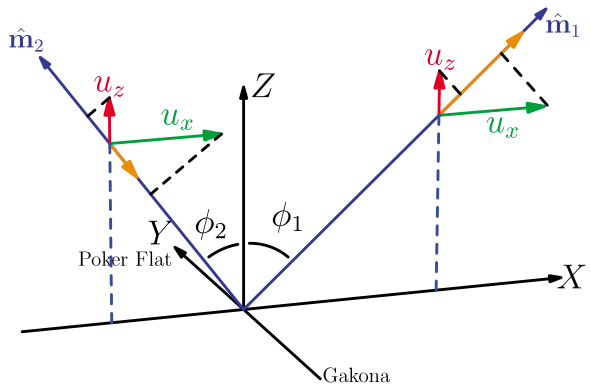

Figure 2. Geometry of the bistatic $\hat{\mathbf{m}}$-component measurement. A horizontal wind u_x (green) and vertical wind u_z (red) are measured as a positive **m** component (orange) on the $+x$ side and negative on the $-x$ side of the y-axis (corresponding to two different values of ϕ, and therefore two different common-volumes). The orange arrows show the line-of-sight component of the wind due to the two-dimensional vector wind whose components are shown by the green and red arrows. The x-y coordinate system is the same as shown in Figure 1.

[19] For a given $\mathbf{u} = (u_m, u_l)$, let the corresponding (horizontal) wind vector relative to the grid axes be labeled $\mathbf{u}_h = (u_X, u_Y)$. Given that the $\hat{\mathbf{l}}$-axis is horizontal, has a constant absolute orientation, and is parallel to the grid Y-axis, the u_l component can be used directly to obtain u_Y, and quintic polynomial interpolation (and extrapolation where grid points are not bounded by measurements) used to fill in the grid squares which do not contain a bistatic measurement.

[20] The u_X component (which is entirely horizontal) could not be calculated directly from u_m, given the variable orientation of the $\hat{\mathbf{m}}$ axis. Referring to Figure 2, for a given grid coordinate Y, the measured u_m component is given as a function of X by the following:

$$u_m(X) = u_X(X)\mathrm{sgn}(X)\sin(\phi(X)) + u_Z(X)\cos(\phi(X)) \quad (3)$$

where $\phi(X)$ is the zenith angle to the point at X and u_Z is the local vertical wind. The sign function sgn(X) is required because the zenith angle $\phi(X)$ has been chosen to be strictly positive, and the measured u_m component of a wind directed along the positive X-axis is negative when looking in the negative X-direction (see Figure 2, where measurements are shown on both sides of the Y-axis, corresponding to two different values of ϕ). We wish to find $u_X(X)$ such that equation (3) is (approximately) satisfied in a best-fit sense.

[21] We do this by first interpolating the measured u_m in the same manner as when gridding u_l, giving us a regular grid of u_m values (example raw u_m measurements are shown in Figure 1 (middle)). We then approximate $u_X(X)$ for each grid row Y by a third-order Taylor expansion about $X = 0$, and make the further assumption that $u_Z(X) = u_{Z0}$ is a constant function of X (but not Y). By making u_Z constant along X, and not, for example, along the magnetic zonal direction, we avoid coupling the Taylor expansion between rows of the grid, which expedites the fitting procedure described below. We then have:

$$u_X(X) \simeq a_0 + a_1X + a_2X^2 + a_3X^3 \quad (4)$$

$$u_Z(X) \simeq b_0 \quad (5)$$

where:

$$a_0 = u_{X0}, b_0 = u_{Z0}$$
$$a_1 = \frac{\partial u_X}{\partial X}, a_2 = \frac{\partial^2 u_X}{\partial X^2}, a_3 = \frac{\partial^3 u_X}{\partial X^3} \quad (6)$$

We then seek to find the set of coefficients $\{a_0, a_1, a_2, a_3, b_0\}$ such that:

$$\tilde{u}_m(X) = \left(a_0 + a_1X + a_2X^2 + a_3X^3\right)\mathrm{sgn}(X)\sin(\phi(X)) + b_0\cos(\phi(X)) \quad (7)$$

is a 'best-fit' to the gridded u_m values in each row of the grid. We achieve this with a least squares fit of equation (7) to the interpolated u_m values (with the individual data points weighted by the inverse of their uncertainties), separately for each row of the grid. The interpolation step is performed prior to fitting so that each row of the grid can be treated independently when fitting equation (7), in order to retain as much independent information as possible. Initial estimates of the b_0 coefficient are obtained from the u_m component interpolated to the Poker/Gakona great circle (at which location u_m is the vertical wind). Final (fitted) estimates of b_0 can be compared with the bistatic vertical winds measured at each of the common-volume locations described in Paper 2. On a typical night, the RMS difference between the fitted b_0 and measured u_m at these locations is $\sim$7 ms^{-1}.

[22] An example fit is shown in Figure 3 (top), where gridded u_m values are plotted as squares, and the fitted curve (equation (7)) is the solid blue line. The data for this figure are the same as shown in Figure 1 (middle), taken from the middle row of the grid. The dashed red line shows what the u_m component would look like for a constant horizontal wind of $u_X = -100$ ms^{-1}. The coefficients of equation (7) are displayed in Figure 3 (bottom), along with the u_X curve derived from them. Figure 1 (right) shows the grid of u_X derived from the measurements in Figure 1 (middle).

[23] Finite-differencing of the gridded horizontal wind vector components u_X and u_Y along the X and Y axes then yields the bistatic wind gradients relative to the grid coordinate system. Note that since $u_X(X)$ is given by equation (4), $\partial u_X/\partial X$ is actually calculated analytically, using:

$$\frac{\partial u_X}{\partial X} = a_1 + 2a_2X + 3a_3X^2 \quad (8)$$

These gradients can then be rotated into geomagnetic coordinates for comparison with the monostatic gradients. Examples of the gradient maps (in grid coordinates, not geomagnetic) generated using this technique are shown in Figure 4. The panels in this figure show, from left to right, the gradient maps of $\partial u_X/\partial X$, $\partial u_X/\partial Y$, $\partial u_Y/\partial X$ and $\partial u_Y/\partial Y$. The color scale is shown at the bottom of the figure.

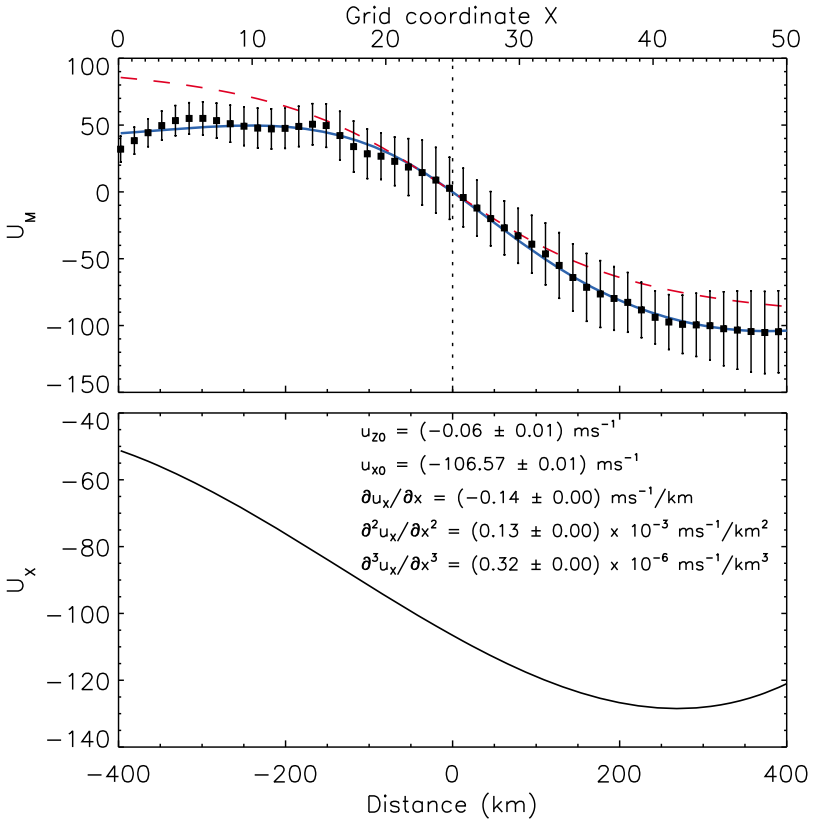

Figure 3. Example showing the least squares fit of equation (7). (top) Data points show the gridded u_m values (from the middle row of the grid in Figure 1, middle), the solid blue curve shows the result of the least squares fit. The 'error-bars' on each data point indicate the relative weighting applied to each data point when performing the fit. The dashed red curve shows how the measured u_m component would appear for a constant horizontal wind of −100 m s^{-1}. (bottom) The fitted u_x from the data in Figure 3, top, with fitted coefficients and uncertainties. Distance is relative to the Gakona/Poker Flat great circle.

[24] The gradient maps in Figure 4 have been spatially smoothed to suppress structures at scales smaller than approximately one quadrant of the grid. Structure at these small scales can easily arise due to the polynomial interpolation of the (spatially) non-uniform distribution of noisy wind measurements, and likely do not represent real, geophysical structure in the gradients. The structures that remain in the maps in Figure 4 show coherent temporal behavior (not shown in this article) which likely reflects real changes in the wind field. For example, when individual gradient maps are viewed as a time-sequence of frames (i.e. as a movie) the spatial structures are observed to vary in a physically plausible manner.

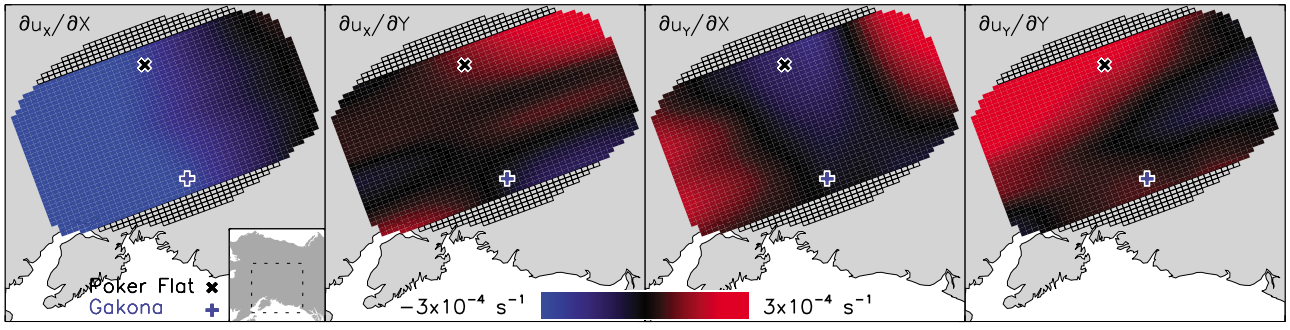

Figure 4. Gradient maps derived from finite-differencing of u_x and u_y. Panels from left to right show respectively the $\partial u_x/\partial x$, $\partial u_x/\partial y$, $\partial u_y/\partial x$ and $\partial u_y/\partial y$ gradients, in grid coordinates (i.e. these have not been rotated into geomagnetic coordinates).

[25] The bistatic gradient calculation is an improvement over the monostatic calculation for two reasons. First, bistatic common-volume wind measurements are *local* in the sense that measurement of a bistatic wind at one location does not rely on a second wind measurement at a different location. The monostatic technique, which relies on the variation of the line-of-sight wind evenly sampled at multiple points around an annulus, cannot be considered local in this sense. An important consequence of the locality of the bistatic measurement is that we are able to generate maps describing the spatial variation of each of the wind gradients, as shown in Figure 4. Of course, the *gridded* horizontal wind components are not strictly local, since they have been interpolated/extrapolated from the measurements onto a regular grid. Additionally, maps of the u_X gradients do not contain as much information as maps of the u_Y gradients, due to the extra assumptions required to obtain u_X from u_m. Even with these caveats, the ability to investigate the spatial structure of the wind gradients represents a big improvement over the monostatic case.

[26] For the gradient examples in Figure 4, the associated wind field was dominated by magnetic westward flow, with the magnitude of the westward flow generally increasing with increasing magnetic latitude. In Figure 4, the grid coordinate Y is aligned within 45 degrees of magnetic westward, and the X coordinate within 45 degrees of magnetic northward. The panel showing the $\partial u_Y/\partial X$ gradient (third panel from the left in Figure 4) therefore shows that while the westward flow was increasing with increasing magnetic latitude at the magnetic north and south edges of the grid (the red areas at the right and left edges of the grid) there was a small region close to the Gakona/Poker Flat great circle where the gradient was actually negative. The monostatic technique cannot resolve such structure and, if validated by further investigation, the gradient maps (of which Figure 4 is just one example) could provide a valuable new data product. While we intend to further examine the gradient fields like those of Figure 4, we have not done so here because we currently have no way to validate this data product.

[27] The second advantage of the bistatic calculation is that it allows estimates to be made of all four gradients. In the monostatic case, only the two gradients describing divergence can be calculated directly. In order to solve for one of the gradients describing shear, a value must be assumed for the other shear gradient, or it must be estimated independently. In the bistatic case, since all gradients are calculated directly, we do not need to make any *a priori* assumptions about any of the gradients themselves. Again, there are some assumptions required in order to derive u_X from u_m, however these assumptions are much less restrictive in terms of the final estimated gradient than is the case with the monostatic assumptions. Bistatic wind imaging therefore allows us to investigate spatial wind structure in much more detail.

[28] The fact that the monostatic and bistatic wind fields show quite close agreement much of the time (see Paper 1, for example) suggests that the gradients estimated using these two different techniques should show a similar level of agreement. While the monostatic wind fit is limited by the assumption of a first-order Taylor wind field and the inability to independently estimate the two shear gradients, the results that we present in the following sections show that these limitations do not greatly affect a single instrument's ability to accurately estimate field-of-view averaged gradients. However, for investigations into the spatial structure of the wind gradients, the extra capabilities afforded by bistatic measurement are required.

4. Results

4.1. Monostatic and Bistatic Gradients

[29] Our primary focus with this study has been to compare grid-averaged bistatic gradients with the gradients routinely calculated using the monostatic technique. This comparison serves two purposes. First, it provides us with a sanity check on the bistatic gradient calculation technique, allowing us to judge the robustness of the algorithm. Secondly, assuming the technique is sound, it gives us insight into the applicability of the monostatic assumption that $\partial v_y/\partial x = 0$.

[30] Comparisons between the monostatic field-of-view averaged and bistatic grid-averaged gradients are shown in Figures 5 and 6. The gradients in these figures have been rotated into geomagnetic coordinates for comparison. Figure 5 displays gradients of the magnetic zonal wind, while Figure 6 shows the gradients of the meridional wind. Poker Flat monostatic gradients are shown as black curves, Gakona monostatic estimates as blue curves, and bistatic estimates as red curves. All curves are plotted as functions of universal time, and magnetic local time is indicated at the top of each figure. Magnetic midnight in the region between Poker Flat and Gakona occurs at approximately 11:10 UT.

[31] Note that the reliability of the bistatic calculation depends rather critically on achieving relatively uniform and complete spatial coverage of the bistatic overlap region. Therefore, only 10 days of data (approximately half of the data set described in Paper 1) are shown in these figures. The date on which the given time series was derived (month and day) is shown on the left side of each figure (all data were recorded during 2010). The scale is indicated by the axis in the center of the figure.

[32] In order to make the comparison as fair as possible, the monostatic $\partial v_x/\partial y$ gradients shown in the right-hand column of Figure 5 have been 'corrected' to include the contribution from the bistatically measured $\partial v_y/\partial x$ gradient. Since the monostatic calculation of $\partial v_x/\partial y$ relies on the assumption that $\partial v_y/\partial x = 0$ in equation (1), the monostatic estimates of this gradient are not directly comparable to the bistatic estimates of this same gradient. Therefore, the bistatic estimates of $\partial v_y/\partial x$ (which the monostatic technique does not measure) have been subtracted from the monostatic estimates of $\partial v_x/\partial y$ in accordance with equation (1). The practical effect of using the bistatic $\partial v_y/\partial x$ gradient to calculate the monostatic $\partial v_x/\partial y$ gradient is investigated in more detail in section 4.2.

[33] It is immediately apparent from these time series data that the bistatic gradient calculation (averaged across the grid) produces gradient estimates that agree well with the monostatic estimates for much of the time. This is not altogether surprising given the often very good agreement observed between the monostatic and bistatic horizontal winds presented in Paper 1. This gives us confidence that the finite differencing approach used to derive the bistatic gradients is a reasonable one. In particular we note that even short-lived features, which frequently have the appearance of

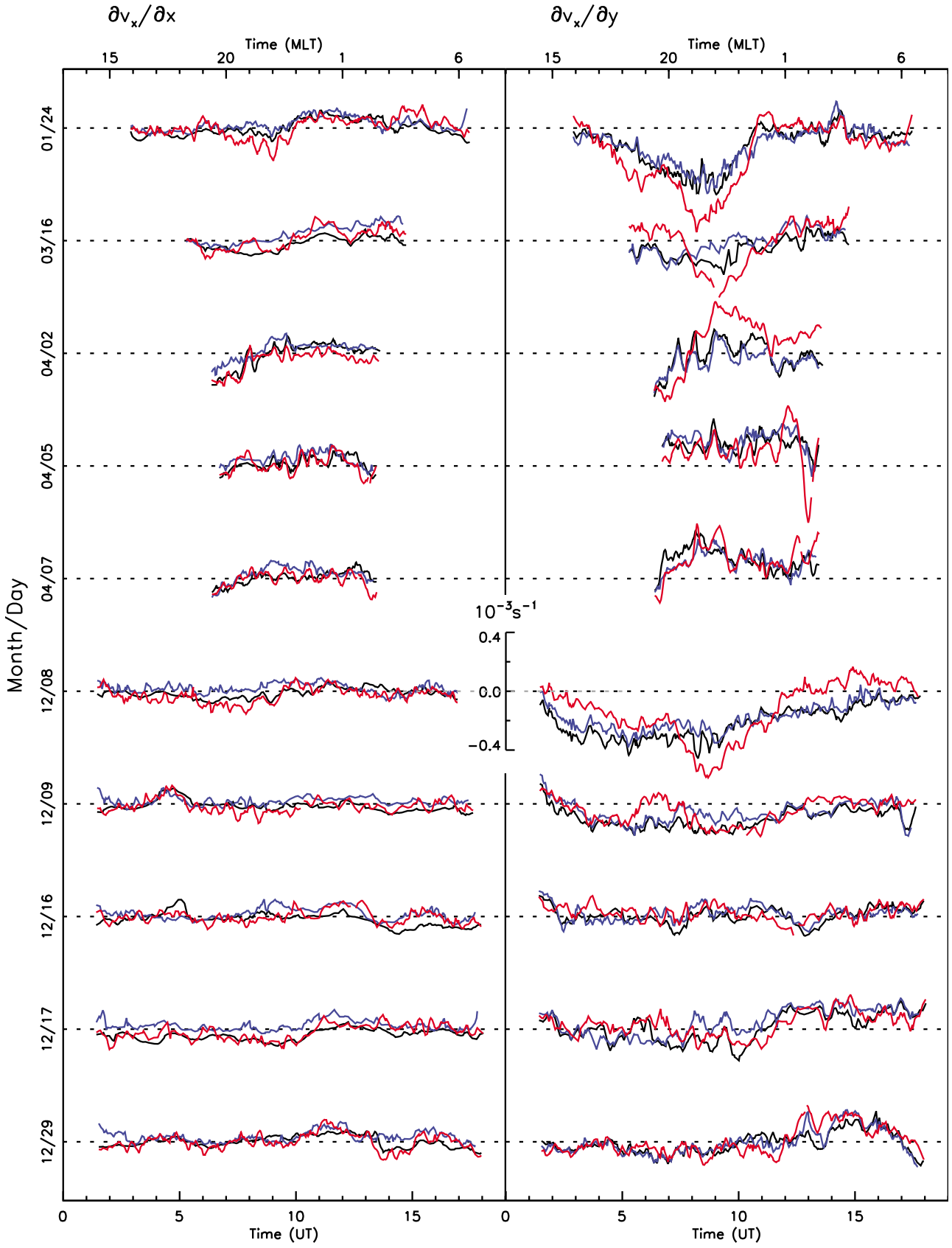
∂v_x/∂x
∂v_x/∂y
Time (MLT)
15
20
1
6
01/24
03/16
04/02
04/05
04/07
12/08
12/09
12/16
12/17
12/29
Month/Day
10^-3 s^-1
0.4
0.0
-0.4
0
5
10
15
Time (UT)

Figure 5

oscillations, are often seen concurrently in both monostatic and bistatic gradient time series.

[34] It is also not uncommon to see the bistatic estimates following the same trend as the monostatic estimates but with a greater magnitude. As for example on 01/24 (January 24, 2010), where the bistatic estimate of $\partial v_x/\partial y$ was considerably larger than both monostatic estimates. This appeared to occur more frequently for the $\partial v_x/\partial y$ gradient than for any other. It is not unreasonable for the bistatic gradients to be larger than the monostatic estimates as they are averaged over a smaller area. The $\partial v_x/\partial y$ gradient is responsible for the large zonal wind shear that is frequently observed in the magnetic afternoon sector, usually collocated with aurora, and which is almost certainly driven by momentum deposition from sunward convecting ions in this sector.

[35] It is also apparent that, for the days presented here, the $\partial v_x/\partial x$ gradient had the smallest magnitude on average. This indicates that zonal divergence is frequently very small. This was not always true for meridional divergence, as for example on 04/05 (April 5, 2010), when meridional divergence was large (up to $\sim 0.4 \times 10^{-3}$ s^{-1}), and displayed oscillatory behavior. This night (April 5, 2010) was examined in some detail in Paper 2, as it was a night of very strong geomagnetic activity, during which time large wave-like oscillations were observed in both the vertical wind and temperature time series, consistent with the presence of gravity waves. If the strong meridional divergence observed on this night was indeed caused by gravity waves (which is likely), the observation of strong meridional divergence and very weak zonal divergence would indicate that the wave phase-fronts were predominantly aligned along the magnetic zonal direction. On nights when activity was not so elevated (during December for example) the meridional divergence was frequently small in magnitude.

[36] In the left-hand column of Figure 6, the bistatically measured $\partial v_y/\partial x$ gradient is shown. Since the monostatic technique assumes that this gradient is zero, for comparison here we have shown the monostatic estimate using the method adopted by *Burnside et al.* [1981]. Using this method, the spectrometer is assumed to be carried by Earth's rotation through a meridional wind field which does not change with local time (over sufficiently short time intervals), and therefore the (same) meridional wind field can be sampled multiple times as the station is carried along the zonal direction [*Conde and Smith*, 1998]. This technique is an alternative to what has been assumed in this work, namely that $\partial v_y/\partial x = 0$. It is shown only for comparison, and at no time does the gradient calculated using the *Burnside et al.* [1981] technique appear in the calculation of any other gradient.

[37] Clearly there are times when the magnitude of the bistatically measured $\partial v_y/\partial x$ gradient is significant, and the validity of the monostatic assumption that $\partial v_y/\partial x = 0$ would be questionable. However, in the monostatic case, the assumption that this gradient is zero only affects the zonal shear gradient. As will be shown in section 4.2, the fact that the zonal shear is often much larger than any of the other three gradients means that in practice the effect of a non-zero $\partial v_y/\partial x$ is often not significant.

[38] These time series also show how the monostatic gradients calculated using the Burnside technique can become unreasonable when the wind field is changing rapidly in local time, as for example on 04/05 (April 5, 2010). A wind field derived using the Burnside-calculated $\partial v_y/\partial x$ would have produced wildly unrealistic structure on this night. Typically, the Burnside technique results in $\partial v_y/\partial x$ gradients which are either very close to zero (when activity is low and the wind field does not change significantly over short time periods), or are large and/or highly oscillatory, in which case wind fields derived from them are often unrealistic. In the first case, the $\partial v_y/\partial x = 0$ assumption is usually reasonable, while in the second case it at least avoids the introduction of large distortions into the derived wind fields.

[39] Divergence and vorticity are often more convenient measures of spatial structure than the individual gradients, and these quantities are shown in Figure 7. As was done for the monostatic $\partial v_x/\partial y$ gradient, the bistatically measured $\partial v_y/\partial x$ gradient has been used to correct the monostatic $\partial v_x/\partial y$ gradient in the calculation of vorticity.

[40] This figure makes it clear that of the two quantities, divergence was much more likely to be small and, at times when it was large, it did not remain so for long periods of time, but instead tended to show oscillatory behavior. Vorticity on the other hand was often large in magnitude, and was more likely to remain large for longer periods of time. Notably, vorticity was often large and positive in the afternoon/evening, due to the relatively frequent occurrence of the strong zonal wind shear that was mentioned previously. In addition, horizontal divergence must be accompanied by vertical transport in order to maintain continuity, and thus divergent flow should be much more difficult to sustain than vortical flow.

4.2. Monostatic Assumption

[41] In the right-hand column of Figure 5, the bistatically calculated $\partial v_y/\partial x$ gradient was used to improve the monostatic estimate of the $\partial v_x/\partial y$ gradient. This was done to provide a fair comparison between the monostatic and bistatic estimates, since the monostatic calculation of this gradient assumes $\partial v_y/\partial x = 0$, which the bistatic analysis has shown is not always a reasonable assumption.

[42] Figure 8 shows the effect of not including the bistatically measured $\partial v_y/\partial x$ in the calculation of the monostatic $\partial v_x/\partial y$. Two panels are shown for each of two days, January 24, 2010 (01/24, top two rows), and December 29, 2010 (12/29, bottom two rows). For each day, monostatic gradients from Poker Flat and Gakona are shown separately. The black curve shows the monostatic $\partial v_x/\partial y$ estimate when the bistatic $\partial v_y/\partial x$ is included (and thus reproduces the result from Figure 5), the green curve shows the estimate when $\partial v_y/\partial x$ is assumed to be zero (the default monostatic assumption), and the red curve shows the bistatically measured $\partial v_x/\partial y$ gradient.

[43] The black curves in this figure show that including the bistatic $\partial v_y/\partial x$ estimate in the monostatic calculation often

Figure 5. Comparison between monostatic and bistatic estimates of the geomagnetic zonal wind gradients. Blue lines show monostatic gradient estimates from Gakona, black lines show monostatic estimates from Poker Flat, and red lines show bistatic estimates. The scale is shown in the center of the figure, and the date is indicated on the left.

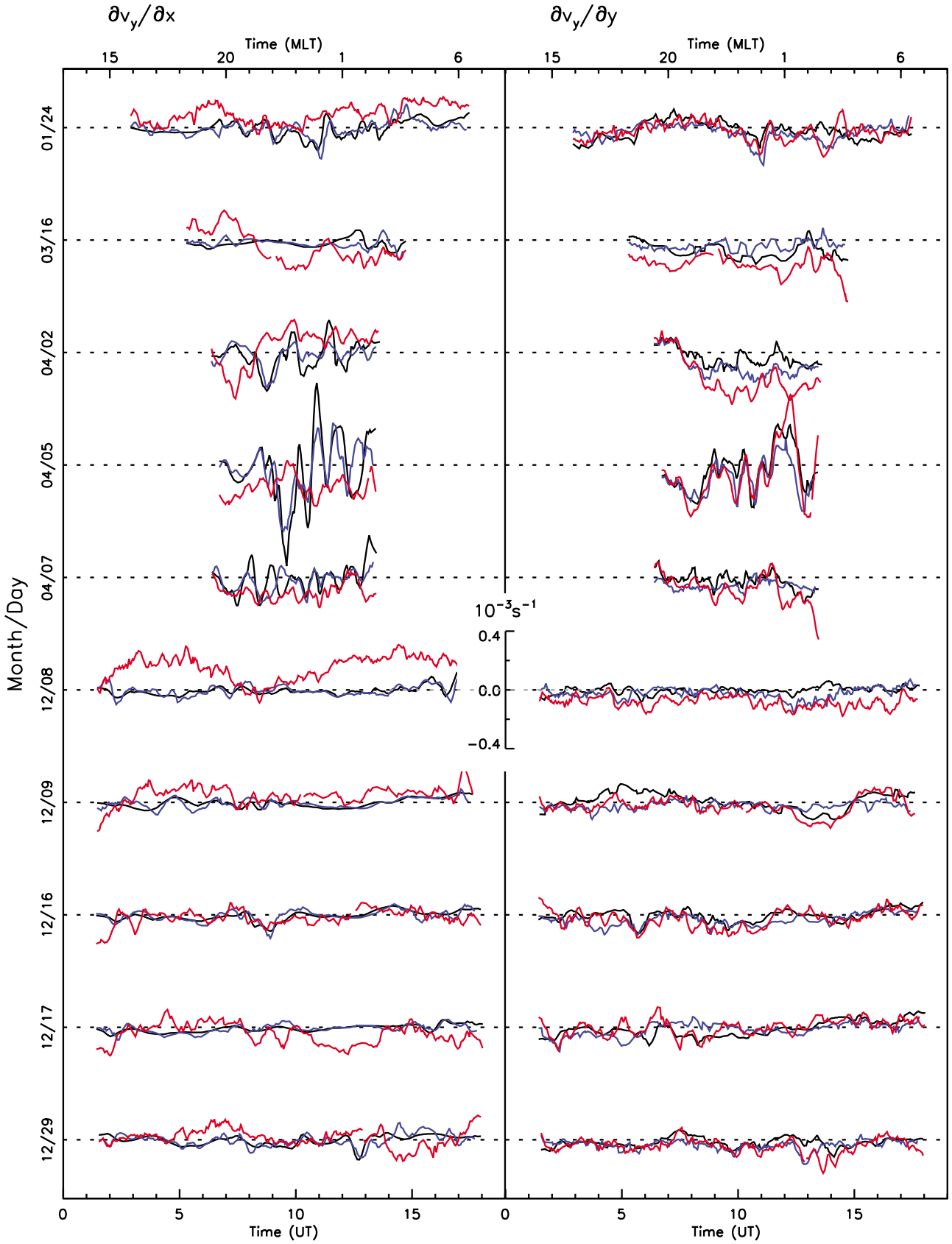

Figure 6. Same format as Figure 5, for estimates of the geomagnetic meridional wind gradients. See text for an explanation of the monostatic $\partial v_y/\partial x$ gradients shown here.

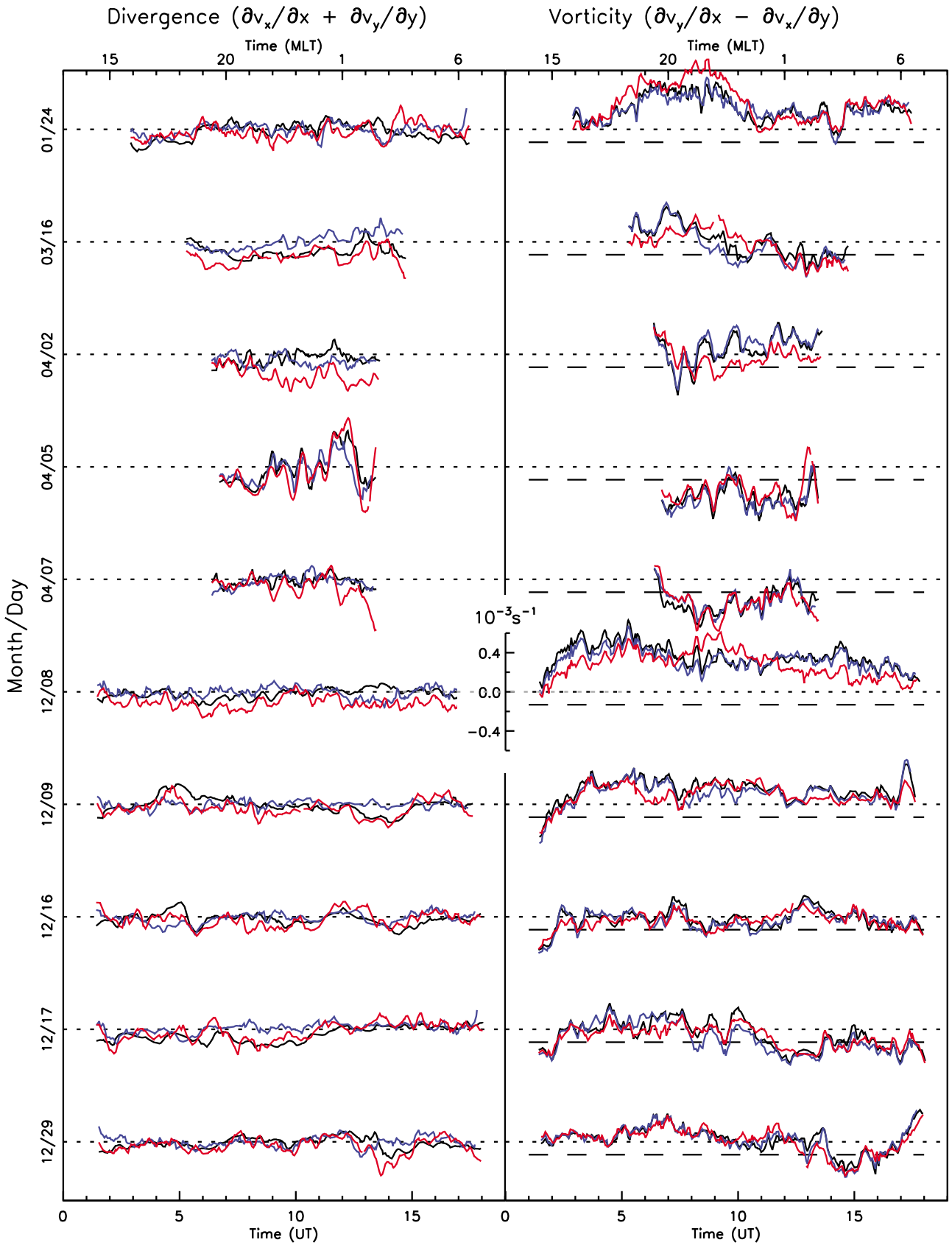
Divergence ($\partial v_x/\partial x + \partial v_y/\partial y$)
Vorticity ($\partial v_y/\partial x - \partial v_x/\partial y$)
Time (MLT)
15
20
1
6
Month/Day
01/24
03/16
04/02
04/05
04/07
12/08
12/09
12/16
12/17
12/29
$10^{-3}s^{-1}$
0.4
0.0
−0.4
0
5
10
15
Time (UT)

Figure 7

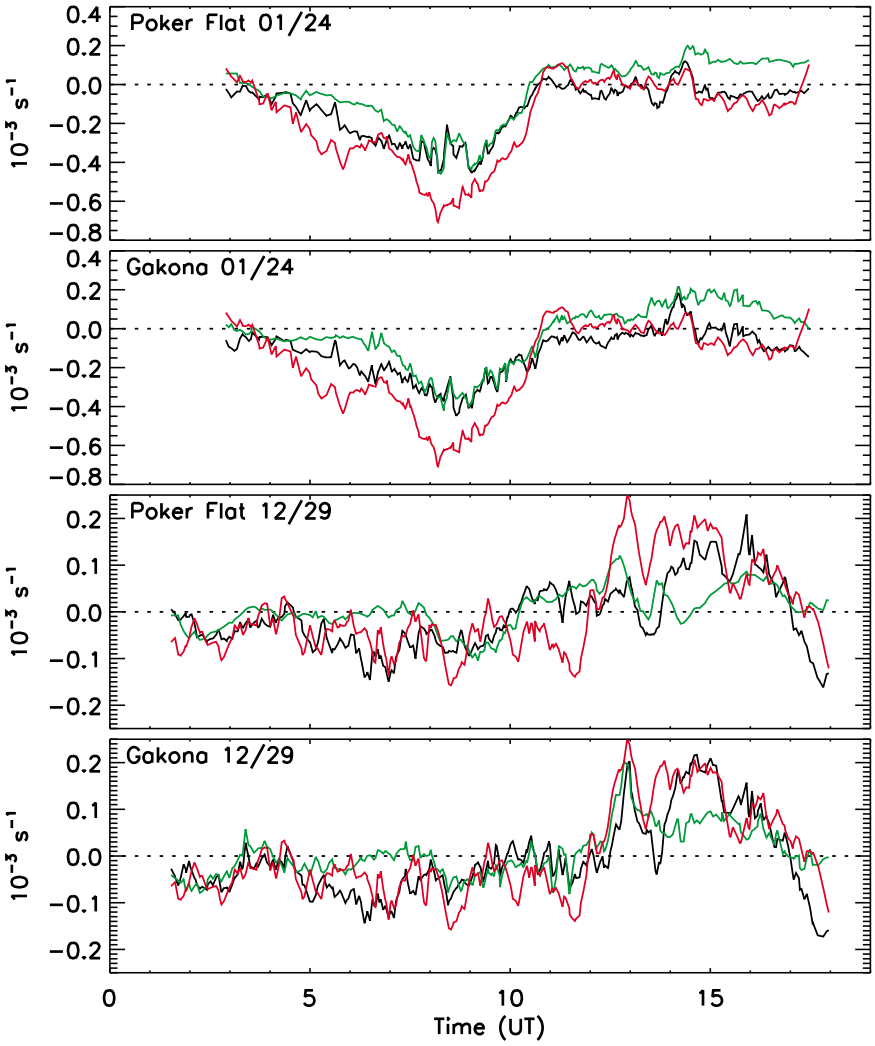

Figure 8. Each panel shows the monostatic $\partial v_x/\partial y$ gradient calculated with the $\partial v_y/\partial x = 0$ assumption (green curve) and calculated using the bistatically measured $\partial v_y/\partial x$ (black curve). The red curve shows the bistatic $\partial v_x/\partial y$ gradient. Comparisons are shown for two days, and for both Poker Flat and Gakona. Note the change in scale between the two days.

improves the agreement between the two data sets. We do not always expect that the magnitude of the monostatic and bistatic gradients should be equal, however, since the monostatic gradients are field-of-view averages, and these fields-of-view are larger than the equivalent bistatic 'field-of-view'. Therefore, while including the bistatic $\partial v_y/\partial x$ estimate can improve the agreement between monostatic and bistatic estimates of $\partial v_x/\partial y$, the value that is used to correct the monostatic estimates may sometimes be too large relative to what the monostatic fit would 'see' if it could measure this gradient directly.

[44] From Figures 5 and 6 we see that often when the bistatic $\partial v_y/\partial x$ estimate is significant, the corresponding $\partial v_x/\partial y$ gradient is also large, and therefore the $\partial v_x/\partial y = 0$ assumption does not significantly affect the resulting wind field in practice. To quantify the effect of this assumption, we have calculated the RMS difference between monostatic and bistatic winds for two cases: monostatic winds derived under the assumption that $\partial v_x/\partial y = 0$ (the default monostatic assumption); and monostatic winds derived using the bistatic estimate of $\partial v_x/\partial y$. The RMS difference in each case was calculated by averaging the squared vector difference over all bistatic measurement locations, and taking the square root. The fractional difference between the two RMS values at each time then quantified the relative impact of the monostatic assumption on the agreement between monostatic and bistatic wind fields. For all of the data presented in Figures 5

Figure 7. Comparison between monostatic and bistatic estimates of the total horizontal divergence and vorticity, in the same format as Figure 5. Note that the scale for these plots (shown in the center of the figure) is slightly larger than for the individual gradient plots. The horizontal dashed line in the vorticity plots indicates the value (-0.132×10^{-3} s^{-1}) below which the flow is inertially unstable (see section 5 of the text).

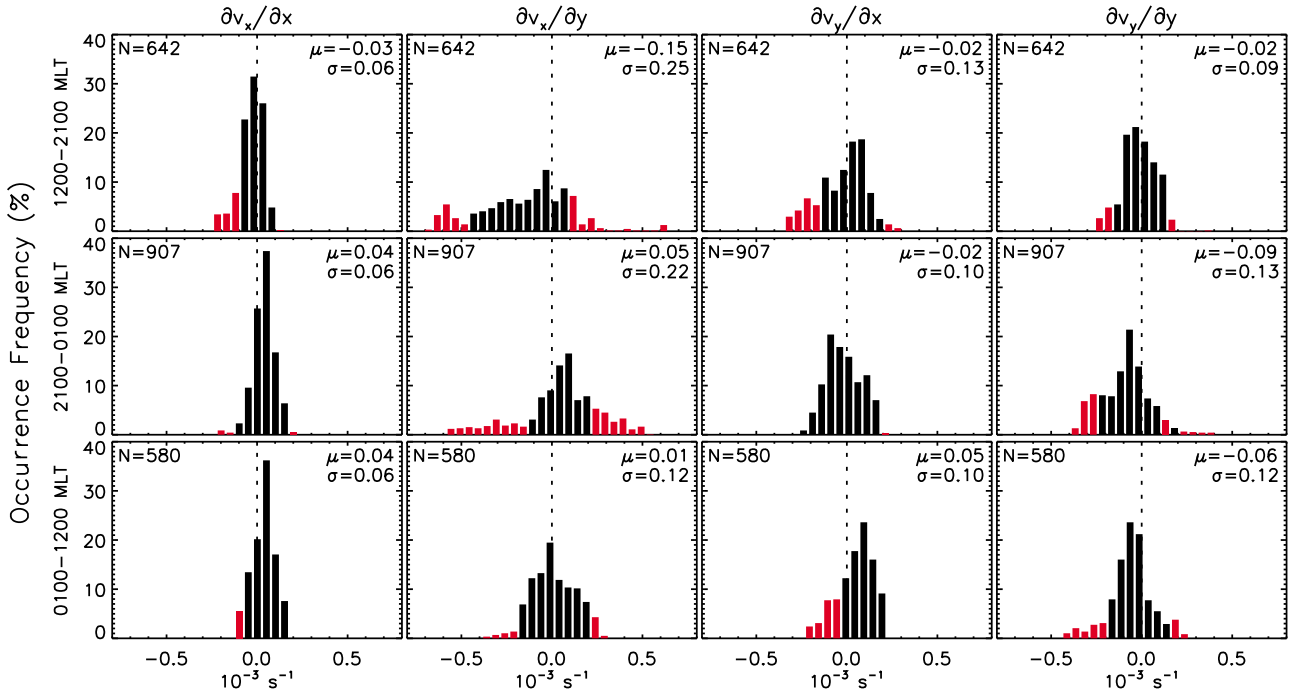

Figure 9. Histograms of the bistatically measured gradients. Panels show the frequency (as a percentage) of observing gradients with the given magnitudes. Distributions have been sorted by magnetic local time sector. Magnetic afternoon and evening (12:00–21:00 MLT) top row, magnetic midnight sector (21:00–01:00 MLT) middle row, and magnetic morning (01:00–12:00 MLT) bottom row. The width of each bin is 0.05×10^{-3} s^{-1}. The number of contributing data points N is shown in the top left of each panel, and data mean (μ) and standard deviation (σ) are shown in the top right. Red bars indicate that fewer than three days of data are included in the bin.

and 6, the mean of the absolute fractional difference was equal to 7.25%.

[45] The agreement between the monostatic and bistatic wind fields is therefore not very sensitive to the $\partial v_x/\partial y = 0$ assumption, since at those times when it may have been significant, the larger shear gradient tends to dominate the structure of the wind field. Of course when the bistatic $\partial v_y/\partial x$ estimate is small, the $\partial v_x/\partial y = 0$ assumption is reasonable in its own right.

4.3. Gradient Distributions

[46] The statistical distributions of the bistatically measured gradients are shown in Figures 9 and 10. Note that more data has been included in these distributions than is shown in Figures 5–7, since periods of good data quality were included regardless of the contiguous length of time those data were available (in the time series figures, days were chosen based on long periods of continuously reliable data). The distributions have been sorted into magnetic local time sectors: magnetic afternoon/evening (12:00–21:00 MLT, top row), magnetic 'midnight' (21:00–01:00 MLT, middle row), and magnetic morning (01:00–12:00 MLT, bottom row). The 19 days from 2010 contributing to these distributions are listed in Table 1.

[47] The choice of the magnetic midnighttime range was based upon two considerations. First, magnetic midnight in the region between Poker Flat and Gakona occurs at approximately 0200 local time, and therefore an even split around magnetic midnight would result in the morning distributions containing less data than the other two sets, due to fewer hours of darkness after this time. Secondly, the magnetic midnight sector as defined here encompasses two hours of observations either side of 23:00 MLT, which *Wang et al.* [2005] have shown is statistically the most likely time for substorm onset to occur. Since substorm onset implies a direct unloading of stored energy into the upper atmosphere, we might expect the thermospheric neutral wind gradients to have different distributions in this time sector. Each panel in Figure 9 shows the (percentage) frequency of occurrence of gradients of the given magnitude. The width of each bin is 0.05×10^{-3} s^{-1}. Bins that are colored red indicate that fewer than 3 unique days of data contributed to the given bin, and should therefore be interpreted with caution.

[48] The distribution of $\partial v_x/\partial x$ reinforces the conclusion that this particular gradient was frequently the smallest in magnitude. It had the lowest standard deviation ($\sigma = 0.06$) of any of the gradients, and was almost completely insensitive

Table 1. The 2010 Bistatic Data Set

Month	Days
January	20th, 23rd, 24th
February	13th, 15th
March	8th, 16th, 31st
April	2nd, 5th, 7th
September	21st, 24th
November	17th
December	8th, 9th, 16th, 17th, 29th

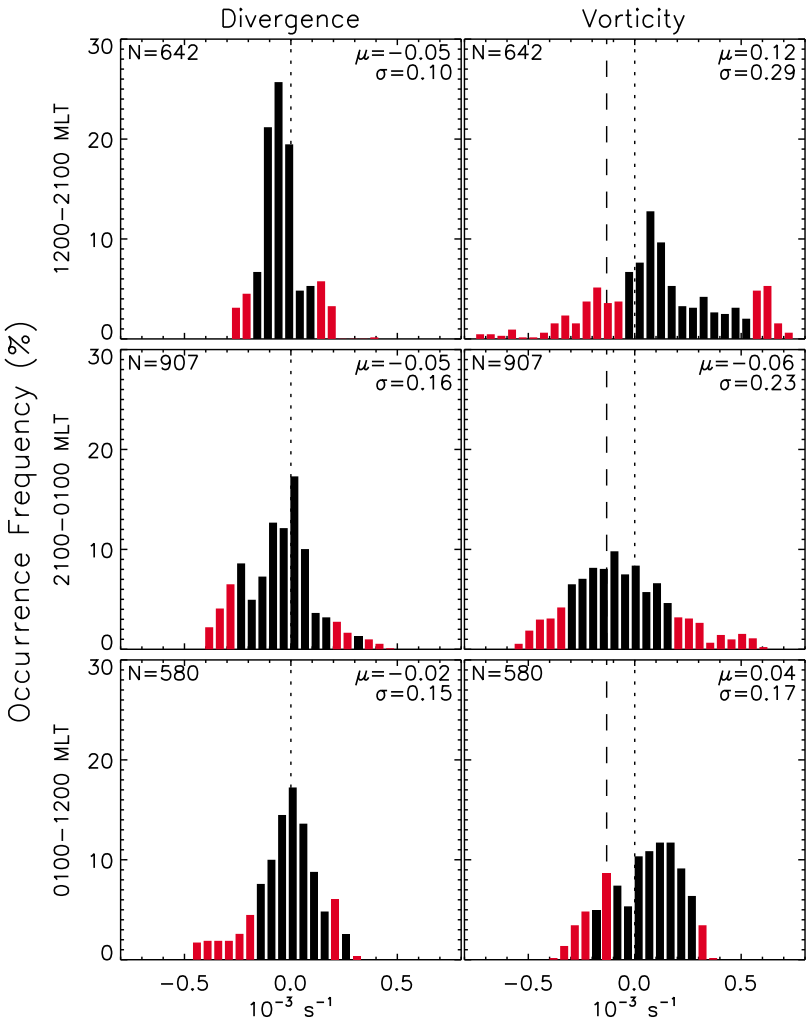

Figure 10. Histograms of the bistatic estimates of divergence and vorticity. This figure is in the same format as Figure 9. The vertical dashed line in the vorticity distributions indicates the value (-0.132×10^{-3} s^{-1}) below which the flow is inertially unstable (see section 5 of the text).

to magnetic local time sector. In contrast, the zonal shear gradient $\partial v_x/\partial y$ had the largest standard deviation, and also showed significant variation with magnetic local time sector. In the afternoon/evening, the distribution was broad and had a negative mean, in agreement with the observation that strong negative zonal shear (magnetic westward flow to the magnetic north, magnetic eastward flow to the magnetic south) is often observed in this time sector. Such a flow configuration is consistent with a convection driven sunward flow to the magnetic north, and pressure-gradient driven antisunward flow to the magnetic south (see Figure 11 for a wind field displaying this type of shear). Interestingly, in the 21:00–01:00 MLT time sector, this gradient had a positive mean, and was skewed more toward positive values, indicating that shear of the opposite sense to that in the afternoon sector was frequently observed between 21:00 and 01:00 MLT. In the morning sector the shear was reduced relative to the earlier times, with a significantly narrower distribution (with approximately half the standard deviation of the 12:00–21:00 MLT distribution) and with a mean closer to zero.

[49] The meridional shear ($\partial v_y/\partial x$) showed clear differences between magnetic time sectors. In the afternoon/evening and morning sectors positive values were more frequently observed, while in the 21:00–01:00 MLT sector negative values were observed more frequently. The distributions were also slightly narrower in the midnight and morning sectors (σ = 0.10) compared to the evening sector (σ = 0.13). The final gradient $\partial v_y/\partial y$ had a narrow distribution in the afternoon/evening sector, and was skewed toward negative values (indicating meridional convergence) in all time sectors.

[50] Figure 10 shows the distributions of the bistatic estimates of divergence and vorticity in the same format as Figure 9. These distributions reinforce the trends which were apparent in the time series plots of Figure 7, and also highlight some important variations with magnetic local time sector. For instance, divergence in the midnight and morning sectors was observed with a larger range of values than in the afternoon/evening, with standard deviations in the last two time sectors approximately 50% larger than that observed in the afternoon/evening.

[51] The vorticity distributions showed some significant differences in each of the magnetic local time sectors. Positive vorticity in the magnetic afternoon and evening was as

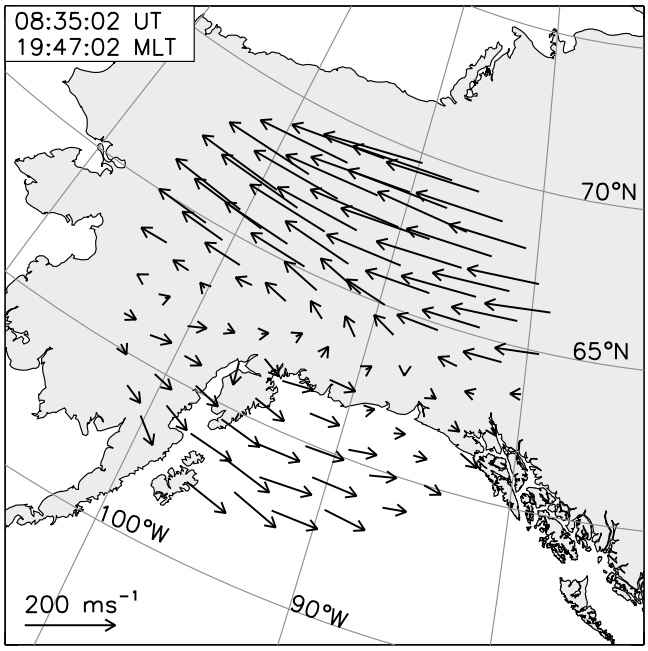

Figure 11. Example of the strongly sheared wind fields which are often observed in the magnetic afternoon time sector, as recorded by the Gakona SDI. The grid and labels indicate geomagnetic latitude and longitude. The universal and magnetic local times are given in the top left of the figure, the wind scale in the bottom left.

expected from the previously mentioned zonal shear which is frequently observed in this time sector. The width of the distribution (approximately 3 times the standard deviation of the divergence in the sector) indicates that vorticity varied rather significantly in the sector. In the 21:00–01:00 MLT sector, the distribution was skewed toward negative values, with a narrower width than in the afternoon/evening sector. In the morning sector, the width was narrower still, and skewed toward positive values.

5. Discussion

[52] Figures 5 and 6 show that calculating thermospheric gradients from bistatically measured winds is feasible, and that the calculated gradients often agree very well with gradients calculated from monostatic measurements. This agreement is reassuring in light of the very different techniques which are used to generate these estimates. In the monostatic case, gradients are calculated directly from Fourier coefficients fitted to the azimuthal variation of line-of-sight wind speed around a measurement annulus centered on just one station. In the bistatic analysis, a process of gridding followed by a weighted least squares fit is required to produce horizontal wind estimates on a regular grid covering the bistatic measurement domain, and the gradients are then calculated by finite-differencing the values in that grid.

[53] The close agreement between estimates derived from these two very different techniques gives us confidence that the gradient estimates reflect structure that is actually present in the wind field, and are not merely artifacts of any single measurement technique. The overall trends highlight the features that are most commonly observed in the wind fields above Poker Flat and Gakona. In particular, the strong zonal shear that is often observed before magnetic midnight above and to the magnetic north of Poker Flat, usually collocated with optical aurora, and often accompanied by magnetic perturbations measured on the ground.

[54] Figures 5 and 6 also show that the thermospheric neutral wind gradients often display systematic variations with local time. April 5, 2010 for example (04/05 in the figures) was a day of strong magnetic activity when wave-like oscillations were observed in vertical winds and temperatures. The gradients on this day (notably $\partial v_x/\partial y$ and $\partial v_y/\partial y$) also showed clear oscillatory behavior, consistent with gravity waves propagating through the field-of-view. There were also times when the magnitudes of all four gradients were relatively small, as for example during the last three days shown from December, when the wind fields were quite uniform over scales as large as the monostatic field-of-view ($\sim$1000 km), and geomagnetic activity was low.

[55] The magnitudes of the observed gradients agree well with the previous estimates mentioned in the introduction. Histograms of gradient values observed in the 19 night data set from 2010 indicate that magnitudes larger than 0.5×10^{-3} s^{-1} were very rarely observed, except in the $\partial v_x/\partial y$ gradient describing meridional shear of the zonal wind in the magnetic afternoon and midnight sectors. This highlights the strong influence that momentum coupling from convecting ions has on the thermosphere above Alaska in these time sectors.

[56] The negative vorticity in the 21:00–01:00 MLT sector may have implications for the development of instability lower down in the thermosphere. *Larsen and Conde* [2011], for example, showed data from the Horizontal E-region Experiment (HEX) rocket campaign, in which a positive zonal wind shear (corresponding to negative vorticity) was observed at an altitude between 130–150 km in the vicinity of an auroral arc. These authors suggested that the magnitude of the meridional gradient of the zonal wind (which contributes to the vorticity) was sufficiently large that the criterion for inertial instability was satisfied. The inertial instability occurs when an initially stable anti-cyclonic (i.e. clockwise in the northern hemisphere) flow becomes unstable to meridional parcel displacements, as the absolute vorticity increases beyond a threshold value [*Larsen and Conde*, 2011].

[57] In Figures 7 and 10, the value of total horizontal vorticity below which the flow is inertially unstable (-0.132×10^{-3} s^{-1} [e.g., *Larsen and Conde*, 2011]) is indicated by a dashed line. The occurrence of vorticity less than this value is not uncommon at F-region heights in the current data set, particulary in the 21:00–01:00 MLT sector (as can be clearly seen from Figure 10). At F-region altitudes, the growth of inertial instability is likely to be damped by viscosity. However, if these types of flows were present at E-region altitudes, the growth of inertial instability may be significant.

[58] While it is not generally known just how far down into the E-region the types of flow structures observed in the F-region can penetrate, examples of very similar E- and F-region flows have been observed by the two instruments used in the current work. If flow structures with negative vorticity were to penetrate down into the E-region, the decreasing influence of viscosity and increasing importance of the Coriolis force may indicate that inertial instability will

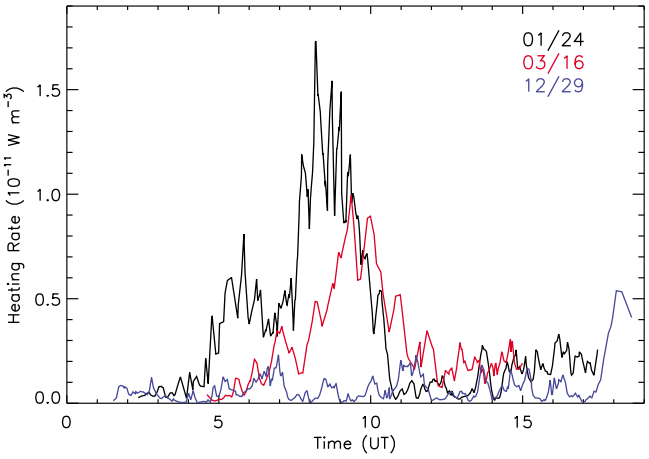

Figure 12. Viscous heating rate per unit volume for January 24 (01/24, black curve), March 16 (03/16, red curve) and December 29 (12/29, blue curve).

be more frequently observed in the 21:00–01:00 MLT sector, at least at the latitude of Poker Flat. Future work will examine bistatic estimates of E-region gradients in order to determine if inertial instability does indeed occur at these lower heights.

[59] The presence of non-negligible gradients in the thermospheric wind field implies that heat will be generated as the mechanical energy of the flow is removed by viscosity. Given the magnitude of the gradients which are sometimes observed, the rate of heating by viscous dissipation can be non-negligible, relative to other sources of neutral heating in the F-region thermosphere. By assuming that all gradients of the vertical wind and vertical gradients of the horizontal wind are negligible, the viscous heating rate can be calculated using [*Rees*, 1989, p. 125]:

$$\frac{\partial q_v}{\partial t} = \eta\left[\left(\frac{\partial v_x}{\partial x}\right)^2 + \left(\frac{\partial v_y}{\partial y}\right)^2 + \left(\frac{\partial v_x}{\partial y} + \frac{\partial v_y}{\partial x}\right)^2\right] - \frac{2\eta}{3}(\nabla\cdot\mathbf{v})^2 \quad (9)$$

[60] A value for the coefficient of dynamic viscosity (η) can be obtained from *Rees* [1989, p. 126], if the neutral temperature and species number densities are known. The NRLMSISE-00 model [*Picone et al.*, 2002] can be used to estimate the number densities, and neutral temperatures are directly measured by the SDIs.

[61] Figure 12 shows the viscous heating rate per unit volume calculated using equation (9), for three of the days shown in Figures 5–7. The largest of these heating rates was on the order of 10^{-11} W m^{-3}, observed on January 24, 2010, driven by a large zonal wind shear in the magnetic evening. This heating rate is likely one or two orders of magnitude lower than typical F-region Joule heating rates [*Hays et al.*, 1973; *Cierpka et al.*, 2000]. Heating rates due to direct particle heating (i.e. neglecting possible contributions to Joule heating through enhancements in conductivity) are of the same order as the largest viscous heating rates derived above [e.g., *Smith et al.*, 1982; *Fujiwara et al.*, 2007]. In addition, since the strongly sheared wind structures can be observed continuously over large regions of local time (in the magnetic afternoon and evening), the time-integrated viscous heating rate can be appreciable [cf. *St.-Maurice and Schunk*, 1981].

[62] We also note that these heating rates were calculated from grid-averaged gradients, under the assumption that vertical wind gradients and vertical gradients in the horizontal wind were negligible. The calculated heating rates therefore represent a lower bound on the actual viscous heating rates that were present.

6. Conclusion

[63] Neutral thermospheric wind gradients have been calculated from bistatic measurements made using two scanning Doppler imagers in Alaska. The key findings from this study are summarized below:

[64] 1. The technique used to calculate gradients from bistatic measurements is robust, and produces gradient estimates which agree closely with monostatic estimates of those gradients most of the time. Bistatic gradients, in particular $\partial v_x/\partial y$, were sometimes larger in magnitude than the corresponding monostatic estimates, a fact that was attributed to the smaller bistatic 'field-of-view' over which these gradients were averaged.

[65] 2. The strongest gradient was $\partial v_x/\partial y$, which describes the meridional shear of the zonal wind. This gradient frequently dominates the structure of the horizontal wind field as it is driven by gradients in plasma velocity. The weakest gradient was $\partial v_x/\partial x$, which describes zonal divergence.

[66] 3. Distributions of divergence and vorticity showed that vortical flow (driven primarily by the aforementioned zonal wind shear) was more commonly observed than divergent flow. Divergent flow was more common after 21:00 MLT than before that time. Vorticity in the magnetic afternoon and morning sectors was more often positive, while in the 21:00–01:00 MLT sector negative vorticity was more frequently observed.

[67] 4. The neutral heating rate due to viscous dissipation of mechanical energy was calculated to be on the order of 10^{-11} W m^{-3}. While small compared to typical F-region Joule heating rates, heating due to viscous dissipation may be comparable to particle heating rates. Given that strong shear is often continuously observed over a large range of magnetic local times in the afternoon sector, the time-integrated heating supplied by this mechanism can be appreciable.

[68] Increasing the size of the bistatic database will be an important goal for future studies utilizing the bistatic technique. With a larger data set, we hope to provide firm statistics for each of the wind gradients, and to analyze their dependence on geophysical parameters such as magnetic and solar activity, and quantify the degree of viscous dissipation that is inevitably associated with gradients in the wind field. With the installation of two additional SDI instruments in the near future, full tristatic observations will be achievable, and will provide exciting new opportunities for future research.

[69] **Acknowledgments.** Gakona SDI installation and operations were supported by Carl Andersen, Tim Manning and Marty Karjala. Poker Flat SDI operations were supported by Carl Andersen, Don Hampton and Brian Lawson. The authors gratefully acknowledge the assistance provided by these individuals.

[70] Robert Lysak thanks the reviewers for their assistance in evaluating this paper.

References

Anderson, C., M. Conde, and M. G. McHarg (2011a), Neutral thermospheric dynamics observed with two scanning Doppler imagers: 1. Monostatic and bistatic winds, *J. Geophys. Res.*, *117*, A03304, doi:10.1029/2011JA017041.

Anderson, C., M. Conde, and M. G. McHarg (2011b), Neutral thermospheric dynamics observed with two scanning Doppler imagers: 2. Vertical winds, *J. Geophys. Res.*, *117*, A03305, doi:10.1029/2011JA017157.

Aruliah, A. L., and E. Griffin (2001), Evidence of meso-scale structure in the high-latitude thermosphere, *Ann. Geophys.*, *19*, 37–46.

Aruliah, A. L., E. M. Griffin, I. McWhirter, A. D. Aylward, E. A. K. Ford, A. Charalambous, M. J. Kosch, C. J. Davis, and V. S. C. Howells (2004), First tristatic studies of meso-scale ion-neutral dynamics and energetics in the high-latitude upper atmosphere using collocated FPIs and EISCAT radar, *Geophys. Res. Lett.*, *31*, L03802, doi:10.1029/2003GL018469.

Aruliah, A. L., E. M. Griffin, A. D. Aylward, E. A. K. Ford, M. J. Kosch, C. J. Davis, V. S. C. Howells, S. E. Pryse, H. R. Middleton, and J. Jussila (2005), First direct evidence of meso-scale variability on ion-neutral dynamics using co-located tristatic FPIs and EISCAT radar in northern Scandinavia, *Ann. Geophys.*, *23*, 147–162.

Biondi, M. A. (1984), Measured vertical motion and converging and diverging horizontal flow of the midlatitude thermosphere, *Geophys. Res. Lett.*, *11*(1), 84–87.

Burnside, R. G., F. A. Herrero, J. W. Meriwether Jr., and J. C. G. Walker (1981), Optical observations of thermospheric dynamics at Arecibo, *J. Geophys. Res.*, *86*(A7), 5532–5540.

Cierpka, K., M. J. Kosch, M. T. Rietveld, K. Schlegel, and T. Hagfors (2000), Direct calculation of F-region Joule heating from simultaneous ion and neutral measurements at high latitudes, *Phys. Chem. Earth (B)*, *25*(5–6), 439–442.

Cole, K. D. (1962), Joule heating of the upper atmosphere, *Aust. J. Phys.*, *15*, 223–235.

Cole, K. D. (1971), Electrodynamic heating and movement of the thermosphere, *Planet. Space Sci.*, *19*, 59–75.

Conde, M., and R. W. Smith (1998), Spatial structure in the thermospheric horizontal wind above Poker Flat, Alaska, during solar minimum, *J. Geophys. Res.*, *103*(A5), 9449–9472.

Conde, M., et al. (2001), Assimilated observations of thermospheric winds, the aurora, and ionospheric currents over alaska, *J. Geophys. Res.*, *106*(A6), 10,493–10,508.

Davidson, P. A. (2004), *Turbulence: An Introduction for Scientists and Engineers*, Oxford Univ. Press, Oxford, U. K.

Friedman, J. F., and F. A. Herrero (1982), Fabry-Perot interferometer measurements of thermospheric neutral wind gradients and reversals at arecibo, *Geophys. Res. Lett.*, *9*(7), 785–788.

Fujiwara, H., R. Kataoka, M. Suzuki, S. Maeda, S. Nozawa, K. Hosokawa, H. Fukunishi, N. Sato, and M. Lester (2007), Electromagnetic energy deposition rate in the polar upper thermosphere derived from the EISCAT Svalbard radar and CUTLASS Finland radar observations, *Ann. Geophys.*, *25*, 2393–2403.

Greet, P. A., M. G. Conde, P. L. Dyson, J. L. Innis, A. M. Breed, and D. J. Murphy (1999), Thermospheric wind field over Mawson and Davis, Antarctica; simultaneous observations by two Fabry-Perot spectrometers of λ630 nm emission, *J. Atmos. Sol. Terr. Phys.*, *61*(146), 1025–1045.

Griffin, E. M., A. L. Aruliah, I. McWhirter, H.-C. I. Yiu, A. Charalambous, and I. McCrea (2008), Upper thermospheric neutral wind and temperature measurements from an extended spatial field, *Ann. Geophys.*, *26*, 2649–2655.

Guo, W., and D. J. McEwen (2003), Vertical winds in the central polar cap, *Geophys. Res. Lett.*, *30*(14), 1725, doi:10.1029/2003GL017124.

Hays, P. B., R. A. Jones, and M. H. Rees (1973), Auroral heating and the composition of the neutral atmosphere, *Planet. Space Sci.*, *21*, 559–573.

Hays, P. B., T. L. Killeen, N. W. Spencer, L. E. Wharton, R. G. Roble, B. A. Emery, T. J. Fuller-Rowell, D. Rees, L. A. Frank, and J. D. Craven (1984), Observations of the dynamics of the polar thermosphere, *J. Geophys. Res.*, *89*(A7), 5597–5612.

Killeen, T. L., and R. G. Roble (1988), Thermosphere dynamics: Contributions from the first 5 years of the Dynamics Explorer program, *Rev. Geophys.*, *26*, 329–367.

Killeen, T. L., P. B. Hays, N. W. Spencer, and L. E. Wharton (1982), Neutral winds in the polar thermosphere as measured from Dynamics Explorer, *Geophys. Res. Lett.*, *9*(9), 957–960.

Killeen, T. L., R. W. Smith, P. B. Hays, N. W. Spencer, L. E. Wharton, and F. G. McCormac (1984), Neutral winds in the high-latitude winter F-region: coordinated observations from ground and space, *Geophys. Res. Lett.*, *11*(48), 311–314.

Larsen, M. F., and M. G. Conde (2011), The Horizontal E-region Experiment: Evidence for inertial instability on the evening side of the auroral oval?, *Geophys. Res. Lett.*, *38*, L17106, doi:10.1029/2011GL048424.

Meriwether, J. W., J. P. Heppner, J. D. Stolarik, and E. M. Wescott (1973), Neutral winds above 200 km at high latitudes, *J. Geophys. Res.*, *78*(28), 6643–6661.

Picone, J. M., A. E. Hedin, D. P. Drob, and A. C. Aikin (2002), NRLMSISE-00 empirical model of the atmosphere: Statistical comparisons and scientific issues, *J. Geophys. Res.*, *107*(A12), 1468, doi:10.1029/2002JA009430.

Rees, M. H. (1989), *Cambridge Atmos. Space Sci. Ser.*, vol. 1, *Physics and Chemistry of the Upper Atmosphere*, Cambridge Univ. Press, Cambridge, U. K.

Smith, M. F., D. Rees, and T. J. Fuller-Rowell (1982), The consequences of high latitude particle precipitation on global thermospheric dynamics, *Planet. Space Sci.*, *30*(12), 1259–1267.

Smith, R. W., and G. Hernandez (1995), Vertical winds in the thermosphere within the polar cap, *J. Atmos. Terr. Phys.*, *57*(6), 611–620.

Spencer, L. E. Wharton, G. R. Carignan, and J. C. Maurer (1982), Thermosphere zonal winds, vertical motions and temperature as measured from Dynamics Explorer, *Geophys. Res. Lett.*, *9*(9), 953–956.

St.-Maurice, J.-P., and R. W. Schunk (1981), Ion-neutral momentum coupling near discrete high-latitude ionospheric features, *J. Geophys. Res.*, *86*(A13), 11,299–11,321.

Wang, H., H. Lühr, S. Y. Ma, and P. Ritter (2005), Statistical study of the substorm onset: its dependence on solar wind parameters and solar illumination, *Ann. Geophys.*, *23*, 2069–2079.

Wu, S. T., S. Matsushita, and L. L. DeVries (1974), An analysis of the upper atmospheric wind observed by LOGACS, *Planet. Space Sci.*, *22*, 1036–1041.